



A two-dimensional model of thermospheric nitric oxide sources and their contributions to the middle atmospheric chemical balance

Francis M. Vitt^{a,*}, Thomas E. Cravens^b, Charles H. Jackman^c

^a*Sterling Software, 1404 Fort Crook Road South, Bellevue, NE, USA*

^b*Department of Physics and Astronomy, University of Kansas, Lawrence, KS, USA*

^c*Laboratory for Atmospheres, NASA/Goddard Space Flight Center, Greenbelt, MD, USA*

Received 8 July 1999; accepted 25 January 2000

Abstract

The NASA/Goddard Space Flight Center two-dimensional (GSFC 2D) photochemical transport model has been used to study the influence of thermospheric NO on the chemical balance of the middle atmosphere. Lower thermospheric NO sources are included in the GSFC 2D model in addition to the sources that are relevant to the stratosphere. A time series of hemispheric auroral electron power has been used to modulate the auroral NO production in the auroral zone. A time series of the Ottawa 10.7-cm solar flux index has been used as a proxy to modulate NO production at middle and low latitudes by solar EUV and soft X-rays. An interhemispheric asymmetry is calculated for the amounts of odd nitrogen in the polar stratosphere. We compute a $< \sim 3\%$ enhancement in the odd nitrogen ($\text{NO}_y = \text{N}, \text{NO}, \text{NO}_2, \text{NO}_3, \text{N}_2\text{O}_5, \text{BrONO}_2, \text{ClONO}_2, \text{HO}_2\text{NO}_2, \text{and HNO}_3$) budget in the north polar stratosphere (latitude $> 50^\circ$) due to thermospheric sources, whereas we compute a $< \sim 8\%$ enhancement in the NO_y budget in the south polar stratosphere (latitude $> 50^\circ$). © 2000 Elsevier Science Ltd. All rights reserved.

1. Introduction

Auroral activity is known to produce huge amounts of nitric oxide (NO) in the Earth's lower thermosphere (on the order of $\approx 10^3$ to $\approx 10^4 \text{ cm}^{-3} \text{ s}^{-1}$) (Townsend and Burke, 1965; Cleary, 1986; Roble et al., 1987; Siskind et al., 1989; Roble, 1992; Barth, 1992). It has been shown that auroral production of NO during geomagnetic disturbances is highly variable and of suf-

ficient magnitude to enhance the globally averaged reservoir of thermospheric NO. During polar night, the aurorally produced NO is long-lived in the thermosphere and may be subject to downward transport into the middle atmosphere where it can couple into middle atmospheric chemistry (Solomon and Garcia, 1984; Roble, 1992; Siskind, 1994; Siskind et al., 1997).

Energetic electrons, both auroral and photoelectrons, produce atomic nitrogen in the thermosphere by ionizing and dissociating N_2 . Atomic nitrogen is quickly converted to NO, which may be transported to the mesosphere and stratosphere if certain conditions are present. The influence of the odd nitrogen ($\text{NO}_y = \text{N}, \text{NO}, \text{NO}_2, \text{NO}_3, \text{N}_2\text{O}_5, \text{BrONO}_2, \text{ClONO}_2,$

* Corresponding author. 1278 Banner Circle, Erie, CO 80516, USA. Tel.: +1-303-828-9681.

E-mail address: francis.vitt@sterling.com (F.M. Vitt).

HO_2NO_2 , and HNO_3) budget in the middle atmosphere by the transport of NO from the thermosphere has been the subject of many studies (Strobel, 1971; McConnell and McElroy, 1973; Brasseur and Nicolet, 1973; Jackman et al., 1980; Solomon, 1981; Solomon et al., 1982; Frederick and Orsini, 1982; Garcia et al., 1984; Solomon and Garcia, 1984; Russell et al., 1984; Brasseur, 1984, 1993; Callis and Natarajan, 1986; Siskind et al., 1989, 1997; Legrand et al., 1989; Garcia and Solomon, 1994). Nonetheless, the contribution of the thermosphere to the odd nitrogen budget of the middle atmosphere has still not been well determined.

Transport processes relevant to the mesosphere and lower thermosphere are not well understood. Siskind et al. (1997) suggest that planetary and gravity waves play a significant role in the transport process. For example, Siskind et al. show that model calculations which consider planetary wave mixing are in better agreement with observations than those which assume a constant horizontal diffusion coefficient. Siskind et al. also point out that these model calculations tend to show a spring time enhancement of NO_y in the stratosphere which is not present in the observations. Their model shows that the aurora contributes much more to the polar stratospheric NO_y budget than the sources associated with solar EUV and soft X-rays at low and middle latitudes and may be an important source of polar stratospheric NO_y . In the current study, we incorporate a time series of solar and auroral activity into a two-dimensional zonally averaged photochemical transport model in order to assess the temporal consequences of including thermospheric sources of NO_y on the chemical budget of the middle atmosphere. The Siskind et al. (1997) model does not incorporate such a time series. We conclude that polar mesospheric NO_y is greatly enhanced during polar night when the downward transport is strongest. We find that thermospheric NO_y may be transported down to ≈ 30 –40 km during the polar night.

2. The model

2.1. Basic two-dimensional model

We use the Goddard Space Flight Center two-dimensional zonally averaged photochemical transport model (GSFC 2D model) which is described by Jackman et al. (1996). The model was first presented by Douglass et al. (1989), but many changes to the model have since been made. The pressure level range was extended through the mesosphere by Jackman et al. (1990). Considine et al. (1994) included heterogeneous chemical processes which occur on the stratospheric sulfate aerosol layer and polar stratospheric clouds and attenuation of solar photon fluxes is now evalu-

ated using a table look-up method (see Jackman et al., 1996).

The model has latitude grid points spaced every 10° , from 85°S to 85°N , and 58 evenly spaced log-pressure grid points positioned approximately every 2 km, from the ground up to approximately 116 km. The daytime averaged values for 62 separate species are computed. A family photochemical approach is used in order to increase the speed of the model. Thirty-two separate families and species are transported. The time step is one day.

The dynamics of the GSFC model has also been significantly improved. Details of the new transport method are briefly described here and by Jackman et al. (1996). The transport fields are prescribed and are derived from empirical data sets in order to maintain the climatological character of the model rather than calculated self consistently as in coupled 2D models. Calculations of the zonally averaged transport fields follow the method used by Garcia and Solomon (1983) and by Bacmeister et al. (1995). Zonal winds (\bar{u}), temperatures (\bar{T}), radiative and latent heating rates, large scale wave induced horizontal diffusion coefficients, and Eliassen–Palm (E–P) flux divergence are all determined off-line from observations as functions of pressure level, latitude, and season. The model then uses the \bar{u} and \bar{T} fields to determine the gravity wave induced vertical diffusion coefficients and the E–P flux divergence for the Lindzen–Holton parameterization. These parameters are then used to solve the meridional streamfunction ($\bar{\chi}^*$) equations to obtain the large-scale

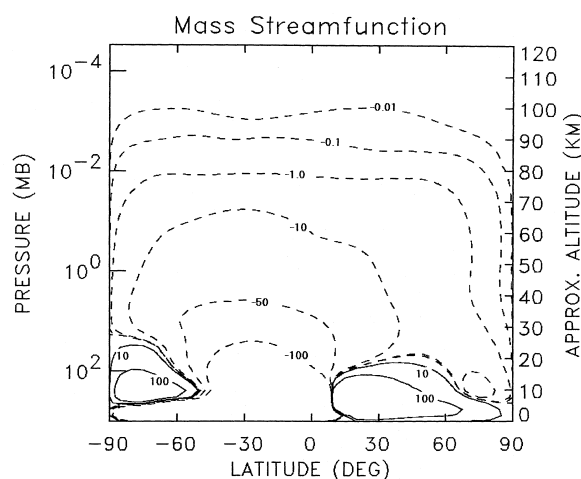


Fig. 1. Contours of the mass meridional streamfunction ($\text{kg m}^{-1} \text{s}^{-1}$) for south polar night conditions; see text. The meridional streamlines coincide with the isopleths of the mass meridional streamfunction. The flow direction is clockwise along the positive contours (solid lines) and is counter-clockwise along the negative contours (dashed lines).

(residual) meridional circulation winds (\bar{w}^* , \bar{v}^*). \bar{w}^* is the residual vertical wind, and \bar{v}^* is the residual meridional wind.

The coefficients of the meridional streamfunction equation depend on calculated zonal wind fields and 17-year average zonal mean temperature fields measured by the National Centers for Environmental Prediction, formerly known as the National Meteorological Center, from the surface (1000 mb) up to the 1 mb level. The CIRA-86 empirical reference model is used for pressure levels less than 1 mb. Zonal winds are computed from temperatures using the gradient wind relation. Forcing of the streamfunction is proportional to the vertical gradient of the mechanical forcing from planetary waves and gravity waves, and the latitudinal gradient of the total heating rate. Diabatic heating rates are calculated using the method of Rosenfield et al. (1994), which includes climatological distributions of temperature, ozone, and water vapor. The climatological latent heating rate distribution is adapted from Newell (1974).

Shown in Fig. 1 are contours of the mass meridional streamfunction, $\bar{\chi}_{\text{mass}}^*$, as described by Garcia and Solomon (1983). This is defined as

$$\bar{\chi}_{\text{mass}}^* = \frac{\rho \bar{\chi}^*}{\cos \theta} \quad (1)$$

where θ is the latitude, ρ is mass density, and

$$(\bar{v}^*, \bar{w}^*) = \hat{i} \times \frac{1}{\rho} \nabla \bar{\chi}^* \quad (2)$$

where \hat{i} is the unit vector in the zonal direction. Hence, the meridional streamlines coincide with the isopleths of the mass meridional streamfunction. The flow direction along the positive contours is in the clockwise direction and along the negative contours is in the counter-clockwise direction. Fig. 1 shows the residual meridional flow directions for mid-July. Note the strong downward motion during polar night from the lower thermosphere to the upper stratosphere over the south pole.

A numerical piecewise parabolic method (PPM) is used to advect the tracers. This advection scheme is based on the method of Lin and Rood (1996), who use the PPM of Colella and Woodward (1984) and Carpenter et al. (1990). This PPM advection scheme is highly accurate and preserves sharp gradients in the tracer distributions.

In order to improve the dynamics, the original GSFC 2D photochemical transport model had been extended from 90 km to about 116 km (from 46 vertical grid points to 58) (Jackman et al., 1996). The region of the model between 90 and 116 km (pressure levels 47 through 58) was treated by Jackman et al. (1996) as a buffer region. The photochemistry of the

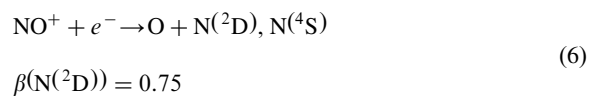
buffer region was not complete; thus computations of constituents in this area were never shown. Here we have remedied this by extending the photochemistry of NO_y up to 116 km. The primary production of thermospheric NO is parameterized as described below.

Chandra et al. (1997) shows that the model does a reasonable job of transporting water vapor throughout the mesosphere. Mesospheric water concentrations are largely controlled by meridional and vertical transport. Chandra et al. (1997) used the GSFC 2D model (essentially the same one we are using for this study) to transport H_2O and found agreement between the model concentrations and concentrations measured by HALOE at 80 km from 1992–1996 to within 10% at 45°N latitude and to within about 20% at 45°S latitude. This agreement supports the validity of the 2D transport scheme we use for the mesospheric region. Comparisons between long-lived stratospheric tracer distributions calculated with the circulation and observations described by Jackman et al. (1996) show that the circulation adequately represents zonal mean transport processes in the middle atmosphere.

In order to improve the speed of the photochemical transport modeling, the GSFC 2D model uses a family chemistry approach to transport the tracers. We solve the continuity equations for only the chemical families rather than for all of the species. Nitric oxide (NO) was transported as part of the NO_x (N, NO, NO_2 , NO_3 , HO_2NO_2) family in the previous version of the GSFC 2D model (see model description on pp. 90–94 in Prather and Remsberg, 1993). Such an assumption breaks down in the upper mesosphere and lower thermosphere where NO can have a long lifetime. The NO produced in the thermospheric auroral zone can be transported down into the mesosphere during polar night. Hence, the GSFC 2D model has been modified to transport NO separately.

2.2. NO_y photochemistry in the lower thermosphere

The production of atomic nitrogen ($\text{N}(^2\text{D})$ and $\text{N}(^4\text{S})$) occurs in the lower thermosphere by the processes



where $\beta(\text{N}^2\text{D})$ is the branching ratio for producing N^2D , e_p^* is an energetic photoelectron, and e_a^* is an energetic auroral electron.

In the lower thermosphere N^2D will produce NO via the reaction



which competes with the quenching reaction



The loss of NO in the lower thermosphere is by the cannibalistic reaction



and by the ionic reaction



See Table 1 for rate constants.

Gerard et al. (1991) assessed the effects of non-thermal (hot) N atoms on NO production in the reaction of ground state N with O_2 and suggested that at equatorial latitudes “this contribution amounts to 6–30% of the other classical production sources of NO for solar minimum conditions.” Below 120 km this source accounts for less than 6% of the total NO production. We do not include this source of NO in our model, which contributes additional uncertainty to our results although only at the few percent level.

2.3. Modeling NO_y photochemistry of the lower thermosphere

We now describe how thermospheric photochemistry is handled in our model. The GSFC 2D model is primarily a middle atmospheric model. We have extended the odd nitrogen photochemistry up to 116 km in order to evaluate the effects of thermospheric odd nitrogen sources on the middle atmosphere. Here we merely seek to provide a reasonable time dependent

upper boundary to a stratospheric photochemical transport model.

2.3.1. Above 90 km

It follows from Eqs. (7) and (8) that the production rate of NO due to thermospheric sources, $P_{\text{NO}}^{\text{therm}}$, will be the production rate of N^2D , $P_{\text{N}^2\text{D}}$ times some efficiency factor, ε , i.e.,

$$P_{\text{NO}}^{\text{therm}} = \varepsilon P_{\text{N}^2\text{D}} \quad (11)$$

where ε , is the ratio of the rate of reaction Eq. (7), (in which N^2D produces NO), to the total loss rate of N^2D . That is,

$$\varepsilon = \frac{k_{\text{N}^2\text{D}+\text{O}_2}[\text{N}^2\text{D}][\text{O}_2]}{k_{\text{N}^2\text{D}+\text{O}}[\text{N}^2\text{D}][\text{O}] + k_{\text{N}^2\text{D}+\text{O}_2}[\text{N}^2\text{D}][\text{O}_2]} \quad (12)$$

$$\varepsilon = \frac{k_{\text{N}^2\text{D}+\text{O}_2}[\text{O}_2]}{k_{\text{N}^2\text{D}+\text{O}}[\text{O}] + k_{\text{N}^2\text{D}+\text{O}_2}[\text{O}_2]} \quad (13)$$

$$\varepsilon = \frac{6 \times 10^{-12}[\text{O}_2]}{1 \times 10^{-12}[\text{O}] + 6 \times 10^{-12}[\text{O}_2]} \quad (14)$$

If we make the very crude estimate that $[\text{O}_2] \approx [\text{O}]$ in the lower thermosphere, then we have, for a rough approximation,

$$\varepsilon \approx 0.86 \quad (15)$$

The remainder of N^2D , which does not produce NO via reaction (7), produces N^4S via reaction (8). Hence the production rate of N^4S via the quenching reaction (8) is $(1 - \varepsilon)P_{\text{N}^2\text{D}}$.

At 110 km ε can vary from ≈ 0.86 to ≈ 0.95 depending on latitude, season, solar activity and geomagnetic activity. In general, ε is greatest at high latitudes during periods of high geomagnetic activity. This range of ε gives more than a factor of two difference in the NO density at 110 km, while in the middle and lower mesosphere the difference is much less. Consequently, the NO production at high latitudes may be

Table 1
Reactions and rate constants for thermospheric NO photochemistry

Reaction	Rate constant ($\text{cm}^3 \text{s}^{-1}$)
$\text{N}^4\text{S} + \text{NO} \rightarrow \text{N}_2 + \text{O}$	$k_{\text{N}^4\text{S}+\text{NO}} = 2.1 \times 10^{-11} \exp(100/T)^a$
$\text{NO} + \text{O}_2^+ \rightarrow \text{NO}^+ + \text{O}_2$	$k_{\text{NO}+\text{O}_2^+} = 4.4 \times 10^{-10b}$
$\text{N}^2\text{D} + \text{O}_2 \rightarrow \text{NO} + \text{O}$	$k_{\text{N}^2\text{D}+\text{O}_2} = 6 \times 10^{-12b}$
$\text{N}_2^+ + \text{O} \rightarrow \text{NO}^+ + \text{N}^2\text{D}$	$k_{\text{N}_2^++\text{O}} = 1.4 \times 10^{-10} \exp(T/300)^{0.44b}$
$\text{N}^2\text{D} + \text{O} \rightarrow \text{N}^4\text{S} + \text{O}$	$k_{\text{N}^2\text{D}+\text{O}} = 1 \times 10^{-12b}$

^a From Table 1 of DeMore et al. (1994).

^b From Table 1 of Barth (1992).

underestimated at times. Improving the parameterization used for the production of NO in the lower thermosphere awaits a more sophisticated model. To simplify chemistry in the upper region of the model, we hold ε constant at 0.86 throughout this study.

The GSFC model does not contain the ions that play an important role in the thermospheric odd nitrogen photochemistry. The production of $N(^2D)$ via ion chemistry associated with the solar EUV and soft X-ray absorption in the low and middle latitudes is characterized by using rates published by Barth (1992) (number of molecules produced or destroyed per unit time per unit volume). The profiles of the rates of reactions (3), (5), (6) and (10) are taken from Barth. The rate of the auroral dissociation (4), which depends on auroral electron power, is provided by using the Fuller-Rowell and Evans (1987) statistical ionization model (see Appendix A). We assume 1.25 molecules of $N(^2D)$ and $N(^4S)$ are produced per ionization which respectively have the branching ratios of 0.6 and 0.4.

Let $R_{N_2+e_p^*}$, $R_{N_2+e_a^*}$, $R_{N_2^++O}$, and R_{NO+O_2} be, respectively, the rate profiles (number of molecules produced or destroyed per unit time per unit volume as functions of altitude) of reactions (3)–(6) and (10). Let $f_d(\lambda)$ be the fraction of the 24 h day that is daylight, which is dependent on latitude and season. The Barth rate profiles are for noontime conditions at equinox. Multiplying the Barth rate profiles by $f_d(\lambda)$ will give an estimate of the daytime averaged rates. To account for solar zenith angle, χ , dependence of attenuation of the solar EUV and soft X-rays, the Barth rate profiles are multiplied by a factor of $\cos(\chi)$ (see Brasseur and Solomon, 1984, p. 103). It follows from Eq. (11), that the production rate of NO, P_{NO}^{therm} , in the lower thermosphere is, therefore,

$$P_{NO}^{therm} = \varepsilon(0.6R_{N_2+e_p^*} + R_{N_2^++O} + 0.75R_{NO^++e^-})f_d(\lambda)\cos(\chi) + 0.6\varepsilon R_{N_2+e_a^*} \quad (16)$$

A noontime solar zenith angle is used.

The loss rate of NO in the lower thermosphere is

$$L_{NO}^{therm} = k_{N+NO} + [NO][N(^4S)] + f_d(\lambda)\cos(\chi)R_{NO+O_2^+} \quad (17)$$

It is assumed that $N(^4S)$ is in photochemical equilibrium. Thus above 90 km we have

$$[N(^4S)] = \frac{J_{NO}[NO] + \sum R}{k_{N+NO}[NO] + k_{N+O_2}[O_2]} \quad (18)$$

where

$$\begin{aligned} \sum R \equiv & (0.4R_{N_2+e_p^*} + 0.4R_{N_2+e_a^*} \\ & + 0.25R_{NO^++e^-})f_d(\lambda)\cos(\chi) + (1-\varepsilon) \\ & \times (0.6R_{N_2+e_p^*} + R_{N_2^++O} \\ & + 0.75R_{NO^++e^-})f_d(\lambda)\cos(\chi) \\ & + (1-\varepsilon)0.6R_{N_2+e_a^*} \end{aligned} \quad (19)$$

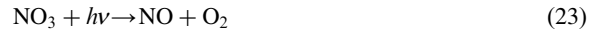
Hence, the loss rate of NO above 90 km can be written as

$$\begin{aligned} L_{NO}^{therm} = & \frac{k_{N+NO}J_{NO}[NO]^2}{k_{N+NO}[NO] + k_{N+O_2}[O_2]} \\ & + \frac{k_{N+NO}[NO]\sum R}{k_{N+NO}[NO] + k_{N+O_2}[O_2]} \\ & + f_d(\lambda)\cos(\chi)R_{NO+O_2^+} \end{aligned} \quad (20)$$

In the thermosphere $[NO_y]$ is assumed to be equal to $[NO]$, so above 90 km the production rate of NO_y is equal to the production rate of NO and the loss rate of NO_y is equal to the loss rate of NO.

2.3.2. Below 90 km

In the middle atmosphere the production of NO is by the processes



and the photochemical sinks of NO are

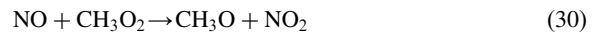
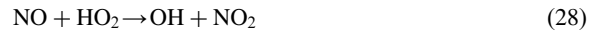


Table 2
Reactions and rate constants^a

Reaction	Rate constant (cm ³ s ⁻¹)
N ₂ O + O(¹ D) → NO + NO	$k_{\text{N}_2\text{O}+\text{O}(\text{D})} = 6.7 \times 10^{-11}$
NO ₂ + O → NO + O ₂	$k_{\text{NO}_2+\text{O}} = 6.5 \times 10^{-12} \exp(-120/T)$
N + OH → NO + H	$k_{\text{N}+\text{OH}} = 5.0 \times 10^{-11}$
NO + N → N ₂ + O	$k_{\text{NO}+\text{N}} = 2.1 \times 10^{-11} \exp(-100/T)$
NO + NO ₃ → 2NO ₂	$k_{\text{NO}+\text{NO}_3} = 1.5 \times 10^{-11} \exp(-170/T)$
NO + HO ₂ → OH + NO ₂	$k_{\text{NO}+\text{HO}_2} = 3.7 \times 10^{-12} \exp(-250/T)$
NO + ClO → Cl + NO ₂	$k_{\text{NO}+\text{ClO}} = 6.4 \times 10^{-12} \exp(-290/T)$
NO + CH ₃ O ₂ → CH ₃ O + NO ₂	$k_{\text{NO}+\text{CH}_3\text{O}_2} = 4.2 \times 10^{-12} \exp(-180/T)$
NO + O ₃ → O ₂ + NO ₂	$k_{\text{NO}+\text{O}_3} = 2.0 \times 10^{-12} \exp(1400/T)$

^a Rates (units of cm³ s⁻¹) are from Table 1 of DeMore et al. (1994).

(See Tables 2 and 3 for reaction rate coefficients and photolysis rates.

Thus, below 90 km the production rate of NO from reactions (21) to (24) in addition to the thermospheric sources, $P_{\text{NO}}^{\text{therm}}$ of Eq. (16), is

$$P_{\text{NO}} = f_d \left(J_{\text{NO}_2} [\text{NO}_2] + J_{\text{NO}_3} [\text{NO}_3] + k_{\text{NO}_2+\text{O}} [\text{NO}_2] \times [\text{O}] + 2k_{\text{NO}_2+\text{O}} [\text{N}_2\text{O}] [\text{O}(\text{D})] \right) + P_{\text{NO}}^{\text{therm}} \quad (33)$$

The loss rate of NO below 90 km from reactions (26) to (32) in addition to the thermospheric sink of ionic reaction (10) is

$$L_{\text{NO}} = f_d (J_{\text{NO}} + k_{\text{NO}+\text{O}_3} [\text{O}_3] + k_{\text{NO}+\text{CH}_3\text{O}_2} [\text{CH}_3\text{O}_2] + k_{\text{NO}+\text{ClO}} [\text{ClO}] + k_{\text{NO}+\text{HO}_2} [\text{HO}_2] + k_{\text{NO}+\text{N}} [\text{N}] + k_{\text{NO}+\text{NO}_3} [\text{NO}_3]) [\text{NO}] + f_d(\lambda) \cos(\chi) R_{\text{NO}+\text{O}_2^+} \quad (34)$$

The evaluation of [N] in this region is done, assuming photochemical equilibrium, in the following way:

$$[\text{N}] = \frac{J_{\text{NO}} [\text{NO}] + \sum R}{k_{\text{N}+\text{NO}} [\text{NO}] + k_{\text{N}+\text{O}_2} [\text{O}_2] + k_{\text{N}+\text{OH}} [\text{OH}]} \quad (35)$$

Table 3
Photodissociations^a

Reaction	Maximum wavelength for photolysis
NO + $h\nu$ → N + O	$J_{\text{NO}} (< 191 \text{ nm})$
NO ₂ + $h\nu$ → NO + O	$J_{\text{NO}_2} (< 400 \text{ nm})$
NO ₃ + $h\nu$ → NO + O ₂	$J_{\text{NO}_3} (< 700 \text{ nm})$

^a The cross sections are taken from DeMore et al. (1994). Gamma bands of NO are taken from Allen and Fredrick (1982).

The largest source of NO_y in the global stratosphere is the oxidation of N₂O, N₂O + O(¹D) → NO + NO (Vitt and Jackman, 1996). N₂O is introduced into the model at the bottom boundary as described by Douglass et al. (1989) and Jackman et al. (1990). There is also a galactic cosmic ray source of NO_y which makes a contribution at high latitudes as described in Vitt and Jackman (1996). Production of NO_y by solar proton events was not included in this particular study.

2.4. Time series of energy inputs

The power inputs into the lower thermosphere, which drive the formation of thermospheric NO, are the solar EUV and soft X-ray radiation and the precipitating auroral electrons in the auroral zone. The solar EUV and soft X-rays have a solar cycle dependence, both 27-day and 11-year. The precipitating auroral electrons depend on auroral activity, which varies greatly from day-to-day.

2.4.1. Solar production of odd nitrogen

The odd nitrogen production associated with solar EUV radiation and soft X-rays is characterized by the rate profile of reactions (10), (3), (5), and (6), denoted as R_i , which we have taken from Barth (1992). These profiles are scaled using the 10.7 cm radio flux parameter, $F_{10.7}$. The time series of $F_{10.7}$ is obtained from The National Geophysical Data Center. The profiles given by Barth are for solar maximum conditions ($F_{10.7} = 200$). Barth et al. (1988) show that nitric oxide in the E-region varies by a factor of ≈ 8 from solar maximum to solar minimum. Thus, we assume that these profiles are reduced to one eighth their maximum strength at solar minimum ($F_{10.7} = 60$). That is, R_i is modulated by

$$R_i = R_i \left(\frac{(F_{10.7} - 60)7}{(200 - 60)8} + \frac{1}{8} \right) \quad (36)$$

2.4.2. Auroral production of odd nitrogen

The odd nitrogen production associated with auroral electrons which are incident on the upper atmosphere is characterized by using a time series of daily averaged hemispheric auroral electron power. This auroral electron power is observed by the TIROS series of satellites (data from Tim Fuller-Rowell and Dave Evans (both at NOAA) (private communication); also see Evans et al. (1987) and Fuller-Rowell and Evans (1987)).

We are able to obtain an ionization profile using a statistical model provided by Fuller-Rowell and Evans (Evans et al., 1987; Fuller-Rowell and Evans, 1987). Given an auroral power and an activity index number, the statistical model returns an ionization profile versus latitude and longitude (see Appendix A for details). These profiles are zonally averaged and input into the 2D model as production rates of $N(^4S)$ and $N(^2D)$. We assume that 1.25 molecules of N ($N(^4S)$ and $N(^2D)$) are produced per ionization (Porter et al., 1976) with the branching ratios of

$$\beta(N(^2D)) = 0.6 \quad (37)$$

$$\beta(N(^4S)) = 0.4 \quad (38)$$

As described above, it is assumed that a fraction of the $N(^2D)$, ε , produces NO, while the remainder $(1 - \varepsilon)$ produces $N(^4S)$.

For time periods where there is no data in the auroral power time series, the K_p index is used as a proxy for estimating the auroral power (see Appendix A). The K_p index is obtained from The National Geophysical Data Center.

2.5. Simulations

The GSFC 2D model has two modes of operation, steady-state and time-dependent. ‘Steady-state’ runs of the 2D model are simulations with fixed boundary conditions. The constituent concentrations calculated by these simulations reach a repeating annual cycle. All steady-state runs in this study are for boundary conditions corresponding to 1970. ‘Time dependent’ runs are simulations where, in addition to the energy inputs, the bottom boundary conditions are determined as functions of time. For example, chlorofluorocarbons (CFCs) are input into the model as bottom boundary conditions which are time dependent.

Time dependent runs include NO production associated with solar EUV and soft X-ray radiation and precipitating auroral electrons as described in Section 2.4. The model runs in this paper do not include solar protons or relativistic electrons.

3. Comparison of results to observations

Nitric oxide in the lower thermosphere and upper mesosphere was observed by the ultraviolet nitric oxide spectrometer (UVNO) experiment on the Atmosphere Explorer D (AE-D) satellite. The UVNO instrument made measurements during the time period from late November 1974 until early February 1975. This was during the minimum of solar cycle 20. Fig. 2(a) shows the NO resulting from the inversion methods described by Cravens et al. (1985).

NO calculated by a run of the 2D model with the time series inputs as described above is shown in Fig. 2(b). This shows NO concentrations for mid-December, 1974. This can be compared to the NO observed by the UVNO experiment of Fig. 2(a). The modeled and observed NO agree reasonably well at high latitudes. At middle and low latitudes the comparison is not good. The model shows a maximum at middle and low latitudes greater than $10^{7.6} \text{ cm}^{-3}$ ($3.98 \times 10^7 \text{ cm}^{-3}$) whereas the UVNO NO is $\approx 10^7 \text{ cm}^{-3}$ at the same latitudes. But, qualitatively, there is a maximum in both NO profiles at $\approx 105 \text{ km}$. In both figures we see a sharp increase in NO in the northern hemisphere as one goes from middle to high latitudes.

The Halogen Occultation Experiment (HALOE) on the Upper Atmospheric Research Satellite (UARS) has also observed NO in the upper mesosphere and lower thermosphere. UARS was launched in September 1991. The HALOE instrument observes several trace constituents of the middle atmosphere via solar occultation. Some data results are presented by Siskind and Russell (1996). Fig. 3(a) shows contours of NO observed during November of 1992. These are zonal means which were constructed by averaging each day’s sunset occultations (up to 15). Fig. 3(b) shows the results of the 2D model during late November of 1992. This figure is compared to Fig. 3(a). Here there is reasonable agreement in the auroral zone in the southern hemisphere. In both figures we also see a deep minimum at approximately 80 km in the middle and low latitudes. Although there is reasonable agreement at $\approx 70 \text{ km}$, our calculation of NO below 60 km overestimates the HALOE NO. In the northern hemisphere, between 70 and 100 km, the contours of the HALOE data slope downward as latitude is increased from 30° to 50°N . This suggests downward transport from the thermosphere. The model results of Fig. 3(b) do not exhibit these downward sloping contours. This is evidence that the model underestimates the downward transport from the lower thermosphere. It should also be noted that the GSFC model computes the species concentrations in daytime averaged form. Hence these model predictions should be closer to the sunset than the sunrise HALOE measurements.

Both Figs. 2 and 3 show model NO concentrations

in the lower thermosphere at low latitudes that are higher than the observed concentrations. The Siskind et al. (1997) model also predicts NO concentrations at low latitudes which are significantly higher than the observed concentrations, but finds better agreement using greater vertical diffusion to bring down more NO to the mesosphere. Vertical mixing associated with gravity waves can penetrate into the lower thermosphere and may not be well represented in this model. We are not able to investigate the effects of using large K_{zz} values ($K_{zz} > 10^6 \text{ cm}^2 \text{ s}^{-1}$) as Siskind et al. (1997) had because numerical instabilities arise in the model associated with the vertical grid spacing. Uncertainties also arise from many other factors, such as the parameterization of the odd nitrogen photochemistry in the lower thermosphere or the scaling of the production rates.

McPeters (1989) gives a time series of NO from 1979 through 1986 in the mesosphere and lower thermosphere which was observed by the solar backscatter ultraviolet (SBUV) instrument on Nimbus 7. Fig. 4 (Figure 8 of McPeters, 1989) shows the observed SBUV column NO above 1 mbar ($\approx 50 \text{ km}$) for five latitude bands: 60°N to 80°N , 40°N to 60°N , 20°N to 20°S , 40°S to 60°S , 60°S to 80°S . Shown in Fig. 5 is

the model predicted column NO above 1 mbar in the same latitude bands for the same time period.

Qualitatively, the trends in the model column NO in the low latitudes agree with the observed column NO. Both Figs. 4 and 5 show a general decrease in the NO columns at low latitudes from 1979 through 1986, from solar maximum to solar minimum. Both Figs. 4 and 5 also show a peak in the NO column at high latitudes near 1982. In the middle and high latitudes the model column NO is generally lower than the observed column NO. For example, the maximum in the model column NO is $\approx 8 \times 10^{14} \text{ cm}^{-2}$ in the 60°N to 80°N region, whereas the observed peak is $\approx 24 \times 10^{14} \text{ cm}^{-2}$. The enhancement at high latitudes in the column NO in July 1982 is due to a fairly large solar proton event in that month. McPeters (1982) used measurements of NO to compute NO column density of $7 \times 10^{14} \text{ cm}^{-2}$ by this solar proton event. Jackman et al. (1990) used measured proton fluxes and an atmospheric model to compute NO column density of $6 \times 10^{14} \text{ cm}^{-2}$ by this solar proton event. The model used in this study does not include the production of NO associated with solar proton events. Also, the parameterization used to model the production of NO in the lower thermosphere may underestimate the production of NO at

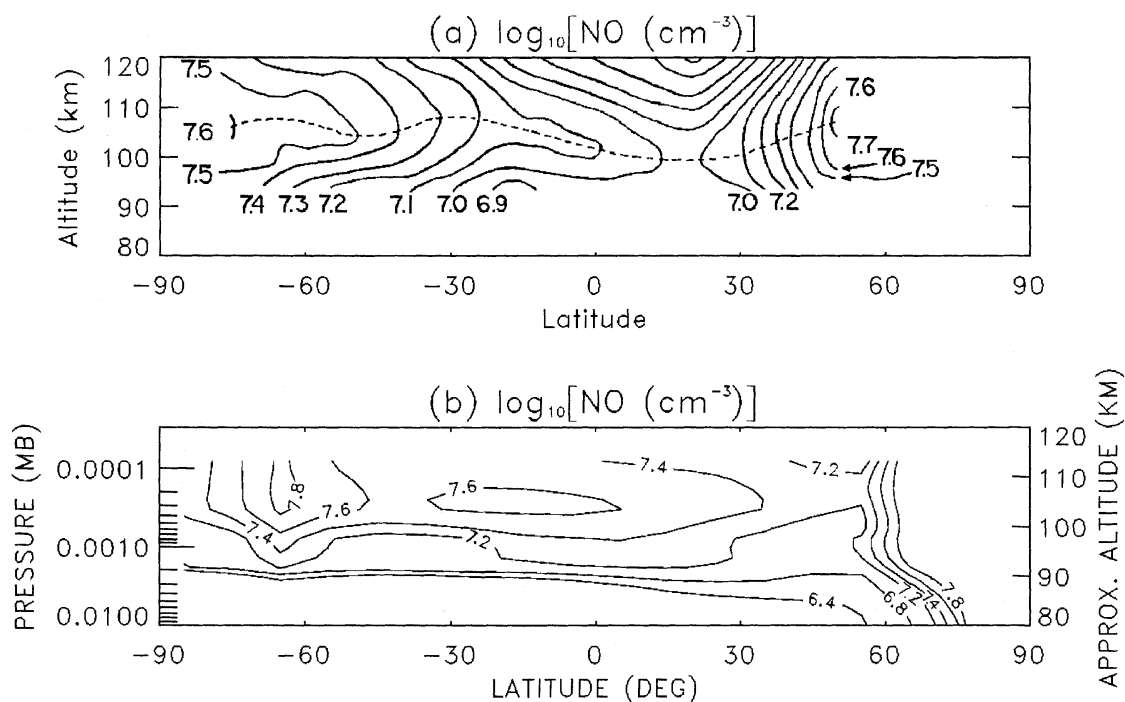


Fig. 2. (a) Extracted from Figure 14 of Cravens et al. (1985). Contour plot of the base 10 log of $[\text{NO}] \text{ (cm}^{-3}\text{)}$ observed during December of 1974 by the ultraviolet nitric oxide spectrometer (UVNO) experiment on the Atmosphere Explorer D (AE-D) satellite. (b) NO concentration at mid-December, 1974, calculated with the 2D model. On this date the hemispheric auroral electron power is 17.7 GW, and $F_{10.7} = 87$. Contour levels are 6.4, 6.8, 7.2, 7.4, 7.6, and 7.8.

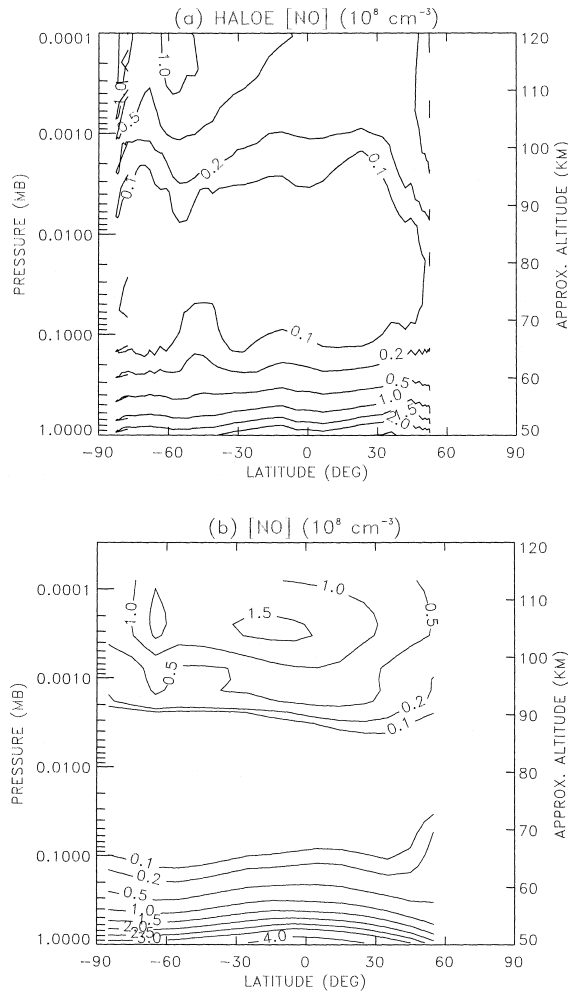


Fig. 3. (a) Contour plot of sunset values of $[\text{NO}]$ (cm^{-3}) observed during November of 1992 by the Halogen Occultation Experiment (HALOE) on the Upper Atmospheric Research Satellite (UARS). (b) NO concentration during late November, 1992, calculated with the 2D model. On this date the hemispheric auroral electron power is 30.9 GW, and $F_{10.7} = 167$.

high latitudes. The value used for ε of Eq. (11) is 0.86. However, this parameter can actually be as high as 0.95 at high latitudes during periods of high geomagnetic activity. Our underestimate of the column NO at these high latitudes may be the result of our upper model boundary at 116 km. Nonetheless, the timing of the high latitude peaks generally coincide with the observations. Hence the temporal variations of the modeled NO above 50 km are in reasonable agreement with the SBUV observed trends and provides a reasonable time dependent upper boundary to our middle atmospheric chemical model.

3.1. Contributions to the chemical budget of the middle atmosphere

In order to quantify the enhancement of the middle atmospheric NO_y from the incorporation of thermospheric sources of NO into the GSFC 2D model, a simulation with the thermospheric sources ('thermospheric simulation') was compared to a simulation without thermospheric sources ('base simulation'). These 25-year simulations are from January 1, 1970, through December 31, 1994.

To assess the effect of thermospheric NO sources on the NO_y budget in various regions of the middle atmosphere, we have calculated the percent enhancement of NO_y in these regions. The percent enhancement is defined as

$$\text{Percent enhancement} \equiv \frac{(N_{\text{therm}} - N_{\text{base}}) \times 100\%}{N_{\text{base}}} \quad (39)$$

where N_{therm} and N_{base} are the integrated total number of molecules in the regions resulting from the thermospheric run and base runs respectively.

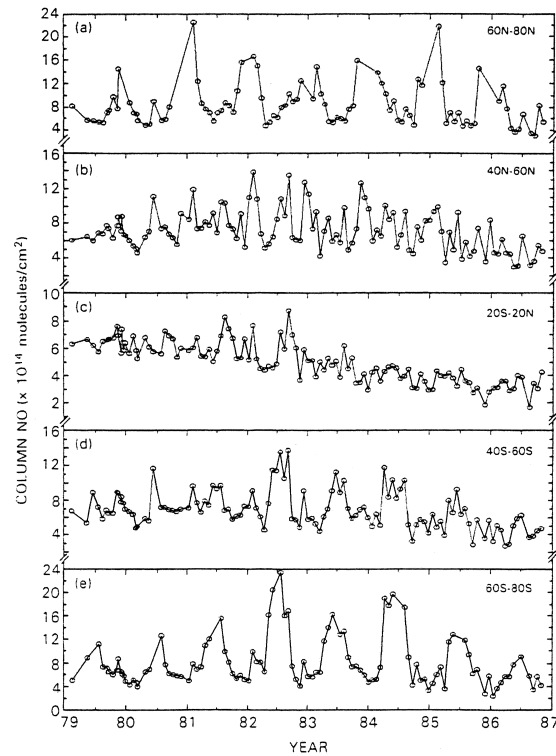


Fig. 4. From Figure 8 of McPeters (1989). The long-term trend in column NO above 1 mbar in units of 10^{14} cm^{-2} for five latitude zones: (a) 60°N to 80°N; (b) 40°N to 60°N; (c) 20°N to 20°S; (d) 40°S to 60°S; (e) 60°S to 80°S.

Fig. 6(a) shows the percent enhancement of NO_y in the north polar mesosphere, between 50° and 90°N latitudes and altitudes between 50 and 90 km. Note the strong dependence of the enhancements on season. The enhancements are predicted to peak during the polar winter (as high as $\approx 800\%$) when the downward circulation is the strongest. The circulation of the 2D model is very strongly dependent on season, and thermospheric NO is long lived during polar night. Hence, the enhancement is strongly dependent on the large scale circulation and thus on the season. There is also an 11-year solar cycle dependence which is evident. This is because the solar EUV, soft X-ray, and auroral sources of NO are dependent on solar activity.

Some of the NO produced in the thermosphere may be transported to stratospheric altitudes where it affects the chemical budget of the middle atmosphere. Fig. 6(b) and (c) show the enhancement of NO_y , defined by Eq. (39) in the north and south polar stratosphere, respectively. The integration for these regions is over latitudes from 50° to the pole, and over stratospheric altitudes (from the tropopause to ≈ 50 km). We compute a stronger enhancement in the southern hemisphere. In the north polar

stratospheric region we compute a $< \approx 3\%$ enhancement, depending on season and year, while in the south polar stratospheric region we compute a $< \approx 8\%$ enhancement. Comparing Fig. 6(b) and (c), one sees that there is a stronger enhancement in the southern hemisphere. Fig. 6(d) shows that the total global stratospheric NO_y budget is enhanced from 1.0% to 2.5% from the addition of the thermospheric sources.

Fig. 7 shows the NO_y mixing ratio (ppbv) for mid-July, southern hemisphere winter. While Fig. 8 shows the percent enhancement of NO_y versus latitude and pressure for mid-July analogous to the calculation of Eq. (39). Again significant enhancements ($> 10\%$) reach down to ≈ 30 km at the south pole during the southern hemisphere winter, when the downward transport is the strongest. During the northern hemisphere winter this significant enhancement reaches down to ≈ 40 km at the north pole.

3.2. Solar cycle variations

The response of the middle atmosphere to the 11-year solar cycle was studied by Garcia et al. (1984) and Huang and Brasseur (1993). Both of these model

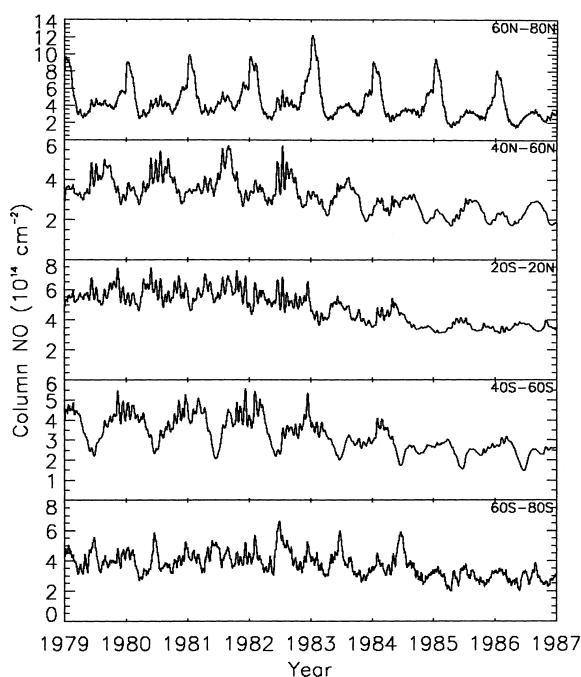


Fig. 5. The modeled long-term trend in column NO above 1 mbar in units of 10^{14} cm^{-2} for five latitude zones: (a) 60°N to 80°N ; (b) 40°N to 60°N ; (c) 20°N to 20°S ; (d) 40°S to 60°S ; (e) 60°S to 80°S .

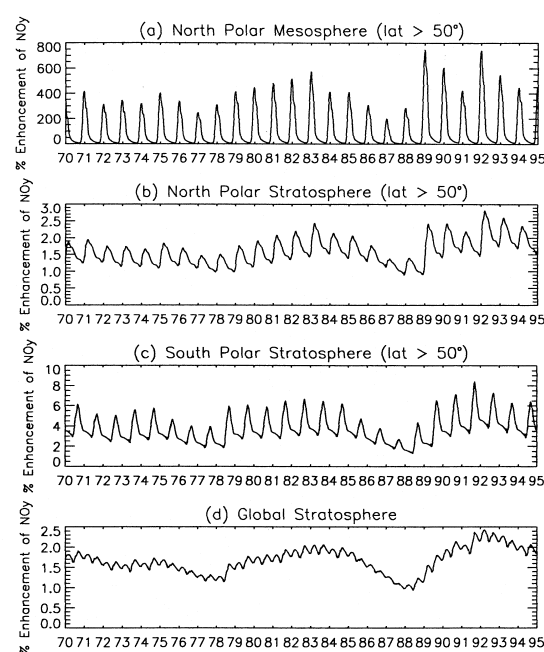


Fig. 6. The percent enhancement of NO_y molecules in (a) the north polar mesosphere (50–90 km), (b) north polar stratosphere (the tropopause – 50 km), (c) south polar stratosphere, (d) global stratosphere due to incorporating the thermospheric sources of NO.

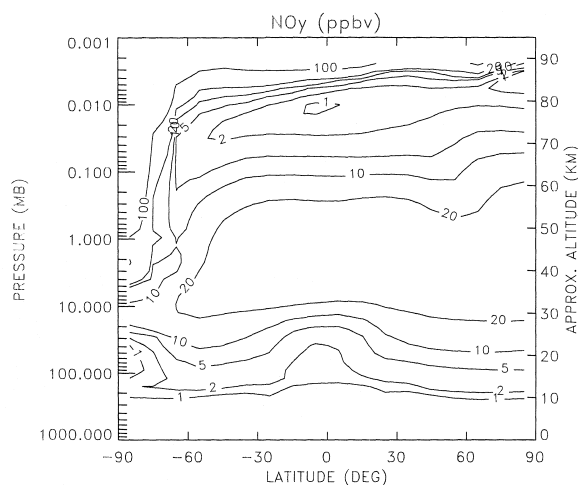


Fig. 7. Modeled NO_y mixing ratio (ppbv) during south polar night. The contour levels are 1, 2, 5, 10, 20, and 100 ppbv.

studies evaluated the NO_y variation between solar maximum and solar minimum times. Figs. 9 and 10 show the percent enhancement in NO_y distribution between solar maximum and solar minimum conditions (1986 and 1989) for late September and late June, respectively. Both Garcia et al. (1984) and Huang and Brasseur (1993) compute an enhancement of $>50\%$ at ≈ 40 km at the south pole during late September. On the other hand, we compute a solar maximum to minimum enhancement of $\approx 30\%$ at 10 mbar (about 32 km). During south polar night, we see

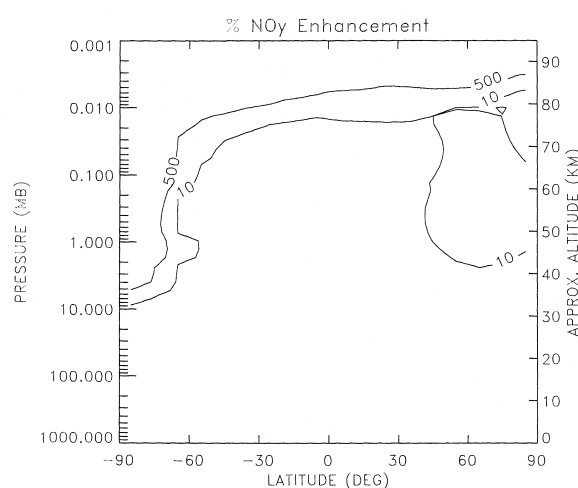


Fig. 8. Percent enhancement of modeled NO_y during south polar night.

a stronger enhancement, of $>100\%$ (see Fig. 10) at 1 mbar.

Garcia et al. (1984) and Huang and Brasseur (1993) both used coupled photochemical transport models and their transport fields vary with the solar cycle since their heating rates are coupled to photochemical budgets which are solar cycle dependent. These other models are used to explore fundamental physical connections. However, our transport fields are independent of solar cycle and only the photochemistry varies with solar cycle. Our transport fields are prescribed based on 17-year climatological data sets which do not vary with the solar cycle. The transport of our model is constrained with empirical inputs for the purpose of being tied closely to observations.

4. Summary and conclusions

The consequences of incorporating thermospheric sources of NO into the GSFC 2D photochemical transport model has been assessed. The enhancement of NO_y in the polar middle atmosphere (produced by thermospheric inputs) is strongly dependent on season. We see an asymmetry with respect to hemispheres, with a stronger enhancement seen at the south pole. During polar night, thermospheric NO is transported down to ≈ 40 km at the north pole and ≈ 30 km at the south pole. The magnitude of the polar night NO enhancement due to the thermosphere strongly

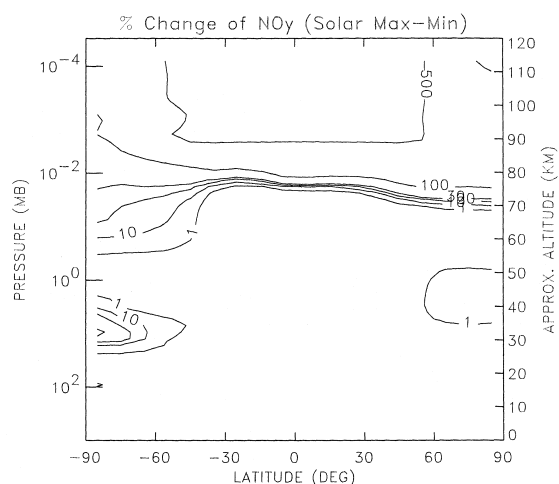


Fig. 9. The percent change in NO_y distribution between solar maximum and solar minimum condition for late September (1986 and 1989). The contour levels are 1%, 10%, 20%, 30%, 100% and 500%.

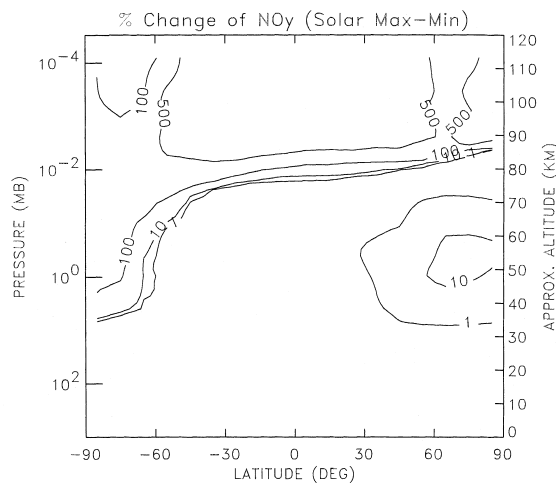


Fig. 10. The percent change in NO_y distribution between solar maximum and solar minimum condition during south polar night (1986 and 1989). The contour levels are 1%, 10%, 100% and 500%.

depends on altitude. Mesospheric NO_y is strongly enhanced during periods when the thermospheric NO downward transport is the strongest, during winter. The modeled column NO_y in the north polar mesosphere is enhanced by as much as $\approx 800\%$, while the modeled column NO_y in the north polar stratosphere is only enhanced by as much as $\approx 3\%$. The model column NO_y in the south polar stratosphere is enhanced by as much as $\approx 8\%$.

Our modeled NO concentrations in the lower thermosphere at low latitude are consistently higher than the observed concentrations. However, our concentrations at high latitudes are more consistent with the observations. The long-term trend of the modeled NO column densities above 1 mbar closely resembles the observations of McPeters (1989) with the exception that our winter time peaks at high latitudes are consistently lower than that of McPeters. We compute south polar NO_y enhancements of 30% at 10 mbar for solar maximum compared to solar minimum. These calculations indicate that significant solar cycle related NO_y

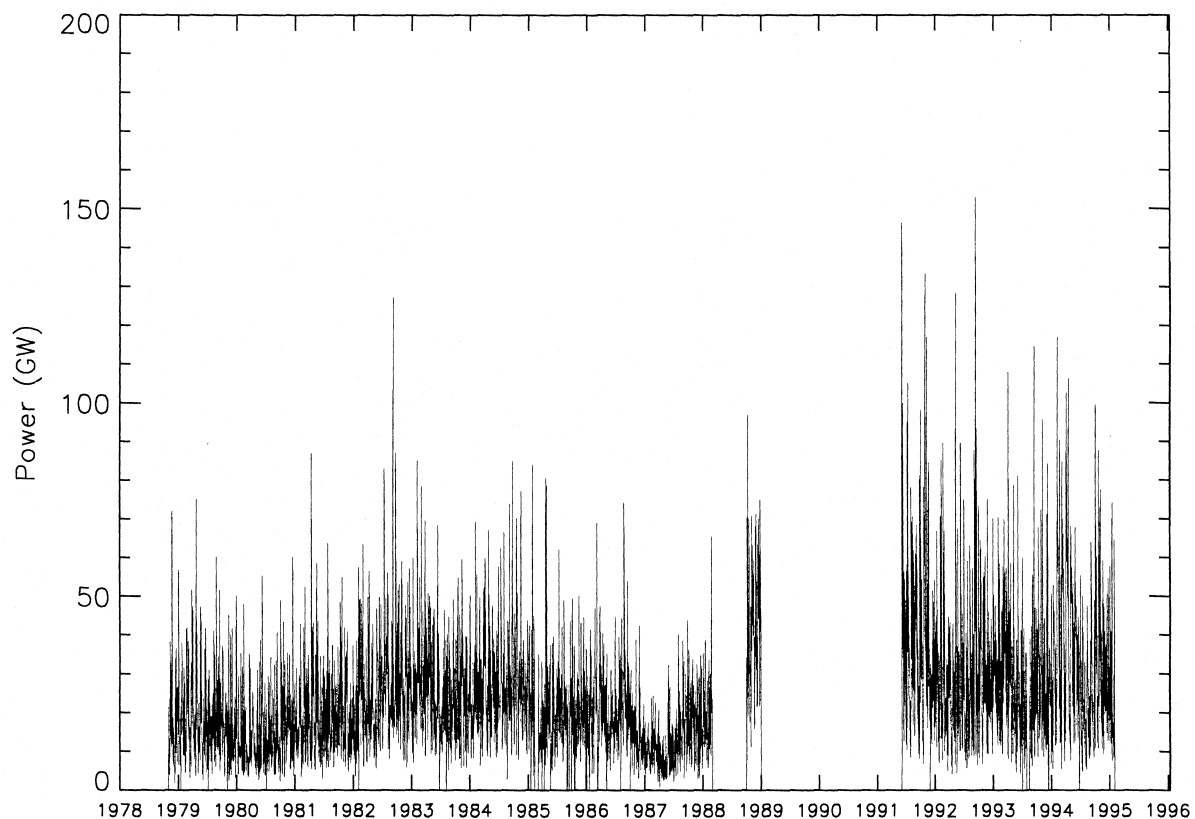


Fig. 11. The daily averaged hemispheric auroral electron power time series.

variations are possible in the mid to upper polar stratosphere.

Acknowledgements

Support for the research is provided by NASA grant NGT 5-3. We thank D.S. Evans and T.J. Fuller-Rowell for the use of the TIROS auroral electron power time series and the use of the statistical auroral ionization model. Useful discussions with T.P. Armstrong and C.A. Barth are also acknowledged.

Appendix A

A.1. Auroral ionization model

Rates of ionization profiles by auroral electron impact in the thermosphere are needed to determine the auroral production rates of odd nitrogen species which are incorporated into the GSFC 2D photochemical model.

Ionization rates are a function of total hemispheric electron power, geomagnetic latitude, and geomagnetic longitude. These rates are independent of ambient density of the atmosphere, and thus independent of model atmosphere, and had been calculated by Tim Fuller-Rowell and Dave Evans at NOAA as described by Fuller-Rowell and Evans (1987) and Evans et al. (1987). Statistical patterns of integrated fluxes of auroral particles and characteristic energies sorted by the time series of electron fluxes measured by TIROS/NOAA polar orbiting satellites are used to calculate the profiles. The TIROS satellites have 11 detector energy passbands. The total energy range of the auroral electrons is from 0.3 keV to 20 keV.

Characteristic energy maps and maps of energy influx into the atmosphere of the auroral particles have been compiled by Evans and Fuller-Rowell for 10 discrete activity levels. The activity levels are determined by total hemispheric auroral electron power. At a particular latitude and longitude the characteristic energy and the integrated energy influx into the atmosphere are determined by the maps, given an auroral activity level. That is, the auroral activity level determines the set of maps to be used. It is assumed that the characteristic energy is sufficient to describe the shape of the energy spectrum and the integrated energy influx is sufficient to normalize the spectrum. A normalized ionization profile is given for each characteristic energy, and the ionization is scaled by the integrated energy influx of the particles. Further, for auroral powers greater than 96 GW, the ionization rates are scaled according to power.

A.2. The auroral power time series

The time series of the hemispheric daily averaged auroral electron power input into the atmosphere starts on day 306, 1978, and runs through day 31, 1995. The time series is shown in Fig. 11. The time series of the Fuller-Rowell and Evans hemispheric auroral electron power has periods where there is no data. In order to remedy this, the daily averaged auroral power has been correlated with the K_p geomagnetic index. We have used K_p as a proxy to fill in the missing gaps of the auroral power time series. The K_p index is linearly correlated with the Fuller-Rowell and Evans hemispheric auroral electron power observations. In addition to filling in the gaps, we can use the proxy to give an auroral power for dates before the start of the time series.

References

- Allen, M., Fredrick, J.E., 1982. Effective photodissociation cross section for molecular oxygen and nitric oxide in the Schumann–Runge bands. *Geophys. Res.* 39, 2066–2075.
- Bacmeister, J.T., Schoeberl, M.R., Summers, M.E., Rosenfield, J.E., Zhu, X., 1995. Descent of long-lived trace gases in the winter polar vortex. *J. Geophys. Res.* 100, 11669–11684.
- Barth, C.A., 1992. Nitric oxide in the lower thermosphere. *Planet. Space Sci.* 40, 315–336.
- Barth, C.A., Tobiska, W.K., Siskind, D.E., Cleary, D.D., 1988. Solar-terrestrial coupling: Low-latitude thermospheric nitric oxide. *Geophys. Res. Lett.* 15 (92).
- Brasseur, G., 1984. Coupling between the thermosphere and the stratosphere: the role of nitric oxide. *MAP Handbook*, vol. 10.
- Brasseur, G., 1993. The response of the middle atmosphere to long-term and short-term solar variability: a two-dimensional model. *J. Geophys. Res.* 98, 32079.
- Brasseur, G., Nicolet, M., 1973. Chemical processes of nitric oxide in the mesosphere and stratosphere. *Planet. Space Sci.* 21, 939–961.
- Brasseur, G., Solomon, S., 1984. *Aeronomy of the Middle Atmosphere*. Reidel, Boston.
- Callis, L.B., Natarajan, M., 1986. The Antarctic ozone minimum: relationship to odd nitrogen, odd chlorine, the final warming, and 11-year solar cycle. *J. Geophys. Res.* 91, 10771.
- Carpenter Jr., R.L., Droegemeier, K.K., Woodward, P.R., Hane, C.E., 1990. Application of the piecewise parabolic method, (PPM) to meteorological modeling. *Mon. Wea. Rev.* 118, 586–612.
- Chandra, S., Jackman, C.H., Fleming, E.L., Russell III, J.M., 1997. The seasonal and long term changes in mesospheric water vapor. *Geophys. Res. Lett.* 24, 639–642.
- Cleary, D.D., 1986. Daytime high-latitude rocket observations of NO γ , δ , and ϵ bands. *J. Geophys. Res.* 91, 11337–11344.
- Colella, P., Woodward, P.R., 1984. The piecewise parabolic

- method, PPM) for gas-dynamic simulations. *J. Comp. Phys.* 54, 174–201.
- Considine, D.B., Douglass, A.R., Jackman, C.H., 1994. Effects of a polar stratospheric cloud parameterization on ozone depletion due to stratospheric aircraft in a two-dimensional model. *J. Geophys. Res.* 99, 18879–18894.
- Cravens, T.E., Gérard, J.C., LeCompte, M., Stewart, A.I., Rusch, D.W., 1985. The global distribution of nitric oxide in the thermosphere as determined by the atmosphere explorer D satellite. *J. Geophys. Res.* 90, 9862–9870.
- DeMore, W.B., Sander, S.P., Golden, D.M., Molina, M.J., Hampson, R.F., Kurylo, M.J., Howard, C.J., Ravishankara, A.R., 1994. Chemical kinetics and photochemical data for use in stratospheric modeling. Evaluation No. 11, JPL Publ. 90-1.
- Douglass, A.R., Jackman, C.H., Stolarski, R.S., 1989. Comparison of model results transporting the odd nitrogen family with results transporting separate odd nitrogen species. *J. Geophys. Res.* 94, 9862–9872.
- Evans, D.S., Fuller-Rowell, T.J., Maeda, S., Foster, J., 1987. Specification of the heat input to the thermosphere from magnetospheric processes using TIROS/NOAA auroral particle observations. *Amer. Astron. Soc.* 65, 1649–1668.
- Fredrick, J.E., Orsini, N., 1982. The distribution and variability of mesospheric odd nitrogen: a theoretical investigation. *J. Atmos. Terr. Phys.* 44, 479–488.
- Fuller-Rowell, T.J., Evans, D.S., 1987. Height-integrated pedersen and hall conductivity patterns inferred from the TIROS-NOAA satellite data. *J. Geophys. Res.* 92, 7606–7618.
- Gerard, J.-C., Shematovich, V.I., Bisikalo, D.V., 1991. Non thermal nitrogen atoms in the Earth's thermosphere 2: source of nitric oxide. *Geophys. Res. Lett.* 18, 1695–1698.
- Garcia, R.R., Solomon, S., 1983. A numerical model of the zonally averaged dynamical and chemical structure of the middle atmosphere. *J. Geophys. Res.* 88, 1379–1400.
- Garcia, R.R., Solomon, S., 1994. A numerical model of the middle atmosphere 2: ozone and related species. *J. Geophys. Res.* 88, 1379.
- Garcia, R.R., Solomon, S., Roble, R.G., Rusch, D.W., 1984. A numerical response of the middle atmosphere to the 11-year cycle. *Planet. Space Sci.* 32, 411–423.
- Huang, T.Y.W., Brasseur, G.P., 1993. Effect of long-term solar variability in a two-dimensional interactive model of the middle atmosphere. *J. Geophys. Res.* 98, 20413–20427.
- Jackman, C.H., Frederick, J.E., Stolarski, R.S., 1980. Production of odd nitrogen in the stratosphere and mesosphere: an intercomparison of source strengths. *J. Geophys. Res.* 85, 7495–7505.
- Jackman, C.H., Douglass, A.R., Rood, R.B., McPeters, R.D., 1990. Effect of solar proton events on the middle atmosphere during the past two solar cycles as computed using a two-dimensional model. *J. Geophys. Res.* 95, 7417–7428.
- Jackman, C.H., Fleming, E.L., Chandra, S., Considine, D.B., Rosenfield, J.E., 1996. Past, present, and future modeled ozone trends with comparisons to observed trends. *J. Geophys. Res.* 101, 28753–28767.
- Legrand, M.R., Stordal, F., Isaksen, I.S.A., Rognerud, B., 1989. A model study of the stratospheric budget of odd nitrogen, including effects of solar cycle variations. *Tellus* 41B, 413–426.
- Lin, S.J., Rood, R.B., 1996. Multidimensional flux-form semi-Lagrangian transport schemes. *Mon. Wea. Rev.* 124, 2046–2070.
- McConnell, J.C., McElroy, M.B., 1973. Odd nitrogen in the atmosphere. *J. Atmos. Sci.* 30, 1465–1480.
- McPeters, R.D., 1982. A nitric oxide increase observed following the July 1982 solar proton event. *Geophys. Res. Lett.* 13, 667–670.
- McPeters, R.D., 1989. Climatology of nitric oxide in the upper stratosphere, mesosphere, and thermosphere: 1979 through 1986. *J. Geophys. Res.* 94, 3461–3472.
- Newell, R.E., Kidson, J.W., Vincent, D.G., Boer, G.J., 1974. *The General Circulations of the Tropical Atmosphere*, vol. 2. MIT Press, Cambridge, MA (Chapter 7).
- Prather, M.J., Remsberg, E.E., 1993. The atmospheric effects of stratospheric aircraft: report of the 1992 models and measurements workshop. NASA Reference Publication 1292, vols. 1–3, NASA Scientific and Technical Information Program.
- Porter, H.S., Jackman, C.H., Green, A.E.S., 1976. Efficiencies for production of atomic nitrogen and oxygen by relativistic proton impact in air. *J. Chem. Phys.* 65, 154–167.
- Roble, R.G., 1992. The polar lower thermosphere. *Planet. Space Sci.* 40, 271–297.
- Roble, R.G., Forbes, J.M., Marcos, F.A., 1987. Thermospheric dynamics during the March 22, 1979, magnetic storm 1: model simulations. *J. Geophys. Res.* 92, 6045–6068.
- Rosenfield, J.E., Newman, P.A., Schoeberl, M.R., 1994. Computations of diabatic descent in the stratosphere polar vortex. *J. Geophys. Res.* 99, 16677–16689.
- Russell III, J.M., Solomon, S., Gordley, L.L., Remsberg, E.E., Callis, L.B., 1984. The variability of stratospheric and mesospheric NO₂ in the polar winter night observed by LIMS. *J. Geophys. Res.* 89, 7267–7275.
- Siskind, D.E., 1994. On the radiative coupling between mesospheric and thermospheric nitric oxide. *J. Geophys. Res.* 99, 22757–22766.
- Siskind, D.E., Russell III, J.M., 1996. Coupling between middle and upper atmospheric NO: constraints from HALOE data. *Geophys. Res. Lett.* 23, 137.
- Siskind, D.E., Barth, C.A., Evans, D.S., Roble, R.G., 1989. The response of thermospheric nitric oxide to an auroral storm 2: auroral latitudes. *J. Geophys. Res.* 94, 16899–16911.
- Siskind, D.E., Bacmeister, J.T., Summers, M.E., Zasadil, S., Russell III, J.M., 1997. Two-dimensional model calculations of nitric oxide transport in the middle atmosphere and comparison with Halogen Occultation Experiment data. *J. Geophys. Res.* 102, 3527–3545.
- Solomon, S., 1981. One- and two-dimensional photochemical modeling of the chemical interactions in the middle atmosphere, 0–120 km). Cooperative Thesis No. 62, University of California and National Center for Atmospheric Research.
- Solomon, S., Crutzen, P.J., Roble, R.G., 1982. Photochemical coupling between the thermosphere and the lower atmosphere 1. Odd nitrogen from 50 to 100 km. *J. Geophys. Res.* 87, 7206–7220.

- Solomon, S., Garcia, R.R., 1984. Transport of thermospheric NO to the upper stratosphere? *Planet. Space Sci.* 32, 399–409.
- Strobel, D.F., 1971. Odd nitrogen in the mesosphere. *J. Geophys. Res.* 76, 8384–8393.
- Townsend, R.D., Burke, J., 1965. Fixation of nitrogen by aurora and its contribution to the nitrogen balance of the Earth. *Nature*, 793–795.
- Vitt, F.M., Jackman, C.H., 1996. A comparison of odd nitrogen production from 1974 through 1993 in the Earth's middle atmosphere as calculated using a two-dimensional model. *J. Geophys. Res.* 101, 6729–6739.